

Andreev Optoelectronics

Benjamin Remez,¹ Pouyan Ghaemi,^{2,3} Jay D. Sau,⁴ and Mohammad Hafezi¹

¹Joint Quantum Institute, University of Maryland, College Park, MD 20742, USA.

²Physics Department, City College of the City University of New York, NY 10031, U.S.A.

³Physics Program, Graduate Center of City University of New York, NY 10031, U.S.A.

⁴Condensed Matter Theory Center and Joint Quantum Institute,

Department of Physics, University of Maryland, College Park, Maryland 20742, USA

(Dated: December 5, 2025)

Superconducting weak-link junctions host electron–hole hybridized excitations called Andreev bound states. These have attracted significant interest for the role they play in the device microelectronic operation and for quantum information applications. Andreev physics has so far been synonymous with the microwave range. However, the maturation of superconductor–semiconductor hybrid junctions opens the door to the characterization, and manipulation, of Andreev states by light. Here we introduce a model for light–Andreev interaction, with distinct features: Electrons transitioning into Andreev levels can sidestep Pauli exclusion, resulting in two optical absorption resonances separated by twice the bound state energy. One resonance populates the Andreev state and the other empties it; pumping both resets the junction and prevents saturation. Given their natural microwave coupling, we show how Andreev bound states can operate as optical–to–microwave transducers. We illustrate these effects with realistic device parameters. Our results highlight the possibilities in the new field of Andreev optoelectronics.

Introduction.—Josephson superconductor–normal-metal–superconductor (SNS) junctions host electron–hole hybridized modes called Andreev bound states (ABSs) [1–4]. These discrete subgap states have attracted attention for novel qubit architectures such as Andreev spin [5–7], level [8, 9], and Majorana qubits [10]. Like other superconducting circuits, Andreev physics is usually studied by its microwave response [11–15]. As ABSs determine the junction Josephson coupling, most recently they have formed the basis for so-called gatemon qubits [16, 17] and other voltage-tunable devices. In these applications, semiconductors are chosen for the junction weak link due to their high electrostatic tunability, and gate-tunable devices have been demonstrated with a variety of semiconductors including InAs [15–20], Ge [14, 21–23], InSb [24–26], and graphene [27–29]. Van der Waals semiconductors like MoS₂ and WSe₂ have also recently been integrated into junctions [30, 31].

Meanwhile, optical control and readout of superconducting microwave circuits has attracted significant attention [32–35] as a key ingredient for quantum networking. However, present conversion schemes [36–41] require additional nonlinear elements for microwave and optical photons to interact [42, 43]. Yet semiconductors underpin optoelectronic and telecoms applications thanks to their moderate band gap in the visible or near-infrared ranges (hereafter collectively termed “optical”). We thus propose that ABSs in semiconductor-based SNS junctions naturally provide a coupling mechanism between the microwave and optical photons.

In this manuscript we put forward a minimal model for light–Andreev interaction, where non-trivial effects are already revealed: First we study how ABSs may be characterized optically by resonant optical absorption, with similarities but also differences to tunneling spectroscopy in Josephson junctions [26, 44–47]. An absorbed photon kicks a valence electron into the conduction band, occupying the Andreev level. Strikingly, since the ABSs are hybridized excitations, an ABS may accept a photoexcited electron whether it is

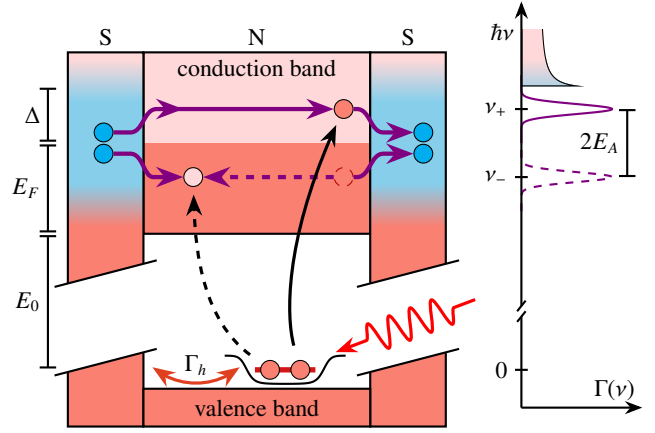


FIG. 1. Sketch of the proposed device band structure and absorption spectrum (not to scale). A doped semiconductor (N, middle segment) with a conduction band Fermi surface (dark pink) is sandwiched between two superconducting leads (S, side segments). In the leads, superconducting pairing opens a gap 2Δ (cyan) around the Fermi level E_F . Far below, the semiconductor valence band is completely filled. A local potential (black dipper) separates a discrete trapped state from the band continuum. Light (red wavy arrow) kicks (black solid arrow) the trapped valence electron into the conduction band. At energies $< \Delta$, this electron (filled circle) hybridizes with a hole below the Fermi surface (empty circle) to form a circulating Andreev bound state (purple). The hole portion of the ABS allows the *occupied* ABS to absorb a second photoexcited electron (dashed black arrow), which we refer to as anomalous absorption. After the two transitions, the junction is reset; in the process, a Cooper pair (blue circles) was photo-injected into one lead. The electron and hole comprising the ABS have kinetic energies $\pm E_A$ relative to the Fermi level, so the absorption resonances of the junction in the empty and occupied states are separated by $2E_A$. The trapped valence orbital overlaps with the leads' conduction band (cut away for clarity) so decays at some rate Γ_h which sets the absorption resonance line widths.

empty or occupied, circumventing Pauli blockade in a mechanism we call “anomalous absorption”. These two transitions are spectrally separated, providing distinct optical knobs to populate and depopulate the junction. This opens the door to time-resolved correlation experiments, manipulating Andreev parity, and shedding light on analogous tangled processes in tunneling spectroscopy [48, 49]. Lastly, by integrating out the Andreev levels we derive an effective transduction Hamiltonian between microwave and optical photons. In this way we show transduction can be accomplished *in situ*, without additional auxiliary systems. Our results, which we group under *Andreev optoelectronics*, highlight semiconductor SNS junctions as a platform for combining circuit quantum electrodynamics with the tools and techniques of quantum optics.

Model.—We sketch the proposed device in Fig. 1. A weak-link SNS junction is formed in a semiconductor whose left and right sides are proximitized by intrinsic superconductors, inducing a gap $\Delta(x)$ in the semiconductor. We assume that the semiconductor geometry and/or global electrostatic doping (global gates not shown) are such that only one transmission channel is active, so the model is effectively one-dimensional. The junction length can be several hundreds of nanometers long, exposing the normal region to illumination. Impinging photons can be absorbed in the semiconductor valence band, exciting electrons into the conduction band, where the Andreev states circulate. This transition is the focus of our manuscript. To resolve it with high spectral sharpness will require a discrete valence level. Such “impurity” states can form naturally in the junction, and can also be intentionally engineered by gating a local electrostatic potential $V(x)$, included in Figure 1 as a shallow trap near the valence band. This provides a discrete valence level isolated from the continuum.

In total, our model Hamiltonian is

$$\hat{H} = (E_0 + E_F)(\hat{h}_\uparrow\hat{h}_\uparrow^\dagger + \hat{h}_\downarrow\hat{h}_\downarrow^\dagger) + E_A(\varphi)(\hat{\gamma}_\uparrow^\dagger\hat{\gamma}_\uparrow - \hat{\gamma}_\downarrow\hat{\gamma}_\downarrow^\dagger) + \hat{V} \quad (1)$$

with the terms representing the valence, conduction, and light-matter interaction Hamiltonians, respectively. We derive this model from a microscopic description in the Appendix. Here $\hat{\gamma}_\sigma^\dagger$ (\hat{h}_σ^\dagger) creates an Andreev quasiparticle (trapped valence electron) with spin $\sigma \in \{\uparrow, \downarrow\}$. We set zero energy at the Fermi level; the distance to the valence state is the optical gap to the conduction band edge E_0 plus the additional conduction band Fermi energy E_F . $E_A(\varphi) > 0$ is the phase-dependent ABS energy; we neglect Coulomb and spin-orbit interactions so the ABSs are spin-degenerate. The model energy hierarchy is $E_A \leq \Delta \ll E_F \ll E_0$ where Δ is the induced superconducting gap deep in the S regions. Note the Andreev operator ordering; here we adopt the convention that excitations only have positive energy, so in its ground state the junction ABSs are both unoccupied. The ground state energy is $-E_A(\varphi)$ and is responsible for the equilibrium Josephson current $I = (2e/\hbar)\partial E_A/\partial\varphi$. For presentational clarity our model contains only one ABS, but the formalism generalizes easily to multiple levels.

The electron field operator $\hat{\psi}_{c\sigma(v\sigma)}$ in the conduction (va-

lence) band is related to the discrete states by

$$\begin{aligned} \hat{\psi}_{c\uparrow}(x) &= u(x)\hat{\gamma}_\uparrow - v^*(x)\hat{\gamma}_\downarrow^\dagger, & \hat{\psi}_{v\sigma}(x) &= f(x)\hat{h}_\sigma. \\ \hat{\psi}_{c\downarrow}^\dagger(x) &= v(x)\hat{\gamma}_\uparrow + u^*(x)\hat{\gamma}_\downarrow^\dagger, \end{aligned} \quad (2)$$

Here $f(x)$ is the valence trapped orbital, while $u(x)$ and $v(x)$ are the particle and hole amplitudes, respectively, of the (up-spin) ABS. u and v are obtained from the Bogoliubov–deGennes (BdG) mean-field Hamiltonian, see the Appendix. Note that $u(x)$, $v(x)$, and $\hat{\gamma}_\sigma$ are implicit functions of φ .

The ABSs and valence holes will have some decay rates, which we denote by Γ_A and Γ_h . We assume that both are slow on the scale of the superconducting gap. As the valence holes will overlap with the conduction band of the leads, we expect them to be comparatively shorter-lived, $\Gamma_A \ll \Gamma_h \ll \Delta$.

We model the light–matter interaction by

$$\hat{V} = g \sum_{\sigma} \int_N dx \hat{\psi}_{c\sigma}^\dagger(x) \hat{\psi}_{v\sigma}(x) \times \alpha e^{-i\nu t} + \text{H. c.} \quad (3)$$

where $\alpha e^{-i\nu t}$ is an external photon field with optical frequency $\hbar\nu \sim E_0 + E_F$ targeting the gap. It may be thought as the coherent mean field of a single optical mode $\langle \hat{a}(t) \rangle$, and we neglected that mode’s spatial structure. That $E_0 \gg \Delta$ permitted a rotating wave approximation and taking the coupling g to be frequency-independent. The subscript N signposts that the integration runs only over the normal region, as we assume the light–matter interaction to be screened in the S regions.

\hat{V} is projected onto the low-energy discrete states by substituting transformation (2), resulting in

$$\hat{V} = [\mathcal{D}_e(\hat{\gamma}_\uparrow^\dagger\hat{h}_\uparrow + \hat{\gamma}_\downarrow^\dagger\hat{h}_\downarrow) + \mathcal{D}_h(\hat{\gamma}_\uparrow\hat{h}_\downarrow - \hat{\gamma}_\downarrow\hat{h}_\uparrow)] \alpha e^{-i\nu t} + \text{H. c.} \quad (4)$$

Here $\mathcal{D}_{e,h}$ are the transition dipole matrix elements given respectively by the ABS electron and hole components,

$$\mathcal{D}_e = g \int_N u^*(x)f(x)dx, \quad \mathcal{D}_h = g \int_N v(x)f(x)dx. \quad (5)$$

Anomalous absorption.—The appearance in Eq. (4) of “anomalous”¹ terms $\propto \mathcal{D}_h$ is the primary novel feature of this section. It shows that valence electrons can be photo-excited into both empty and occupied Andreev bound states, thanks to the latter’s p–h hybridization. This is illustrated in Fig. 1. An electron transitioning into an occupied ABS depopulates it.

This process will be evident in the junction’s light absorption spectrum: At cryogenic temperatures, $E_A \sim \Delta \gg k_B T$ so the Andreev sector is empty, $\langle \hat{\gamma}_\sigma^\dagger \hat{\gamma}_\sigma \rangle = 0$. However, steady-state absorption rates can be computed from ground state expectation values only if the system has sufficient time to dissipate each photon to the environment before the next photon is absorbed. The ABSs are long lived, so irradiation can sustain an out-of-equilibrium nonvanishing ABS population. These will support an anomalous optical transition.

¹ We say anomalous since it is superficially particle-nonconserving.

We treat absorption within Fermi's Golden Rule (FGR), considering an initial Fock state with Andreev occupation $\langle \hat{\gamma}_\sigma^\dagger \hat{\gamma}_\sigma \rangle = n_{A,\sigma}$ and valence occupation $\langle \hat{h}_\sigma^\dagger \hat{h}_\sigma \rangle = n_{h,\sigma}$. The absorption spectrum is given by the FGR transition rate per drive intensity,

$$\frac{\Gamma(\nu)}{|\alpha|^2} = \Gamma_h \times \sum_{\sigma} \left[\frac{|\mathcal{D}_e|^2 n_{h,\sigma} (1 - n_{A,\sigma})}{(\hbar\nu - E_0 - E_F - E_A)^2 + \hbar^2 \Gamma_h^2 / 4} + \frac{|\mathcal{D}_h|^2 n_{h,\bar{\sigma}} n_{A,\sigma}}{(\hbar\nu - E_0 - E_F + E_A)^2 + \hbar^2 \Gamma_h^2 / 4} \right] \quad (6)$$

where $\bar{\sigma}$ means the spin opposite to σ . The two terms in Eq. (6) correspond to the normal and anomalous transitions, producing resonances at photon energies $\hbar\nu_{\pm} = E_0 + E_F \pm E_A$, respectively. Since $\Gamma_h \gg \Gamma_A$, the former sets the Breit-Wigner resonance line widths. Eqs. (2), (4), and (6) are easily generalized to multiple ABS levels and valence orbitals.

That the two transitions involve opposite electron spin, straddle the Fermi level, and reset the ABS, can be understood by considering the electrons' destination: After two transitions, two electrons have been transferred to the conduction band, whereby they pair and enter one of the superconducting leads. Inserting a Cooper pair into the condensate takes twice the chemical potential, and indeed $\nu_+ + \nu_- = 2(E_0 + E_F)$ is twice the position of the Fermi level, measured relative to the valence orbital. A two-photon absorption $\propto |\mathcal{D}_e \mathcal{D}_h|^2$, not included in Eq. (6), will appear at frequency $(\nu_+ + \nu_-)/2$.

This situation is analogous to tunneling spectroscopy, showing twinned differential conductivity peaks at positive and negative voltage. These are commonly associated, respectively, with the ABS electron (u^2) and hole (v^2) components [50]. However, this holds only if that state is strongly dissipated by a fermionic bath [49, 51]. For an isolated (longlived) ABS, particle-hole symmetry implies that the peaks must be equal, and the tunneling $\propto u^2 v^2 / (u^2 + v^2)$ [48] shows the electron and hole components remain intertwined. This is facilitated by similar "anomalous" electron transitions into the occupied ABS. Nevertheless, to the best of our knowledge, the capacity of occupied ABSs to anomalously take in photo-pumped electrons has not been noted before. Moreover, the two optical absorption peaks still map (via $\mathcal{D}_{e,h}$) purely to u and purely to v , even if the ABS is isolated. (The coupling to the valence band is not particle-hole symmetric.)

Eq. (6) gives instantaneous transition rates, and where (the frequency integrated) $\Gamma(\nu)$ lies with respect to $\Gamma_{A,h}$ will determine the steady state: (i) If $\Gamma \ll \Gamma_A$, $n_{A,\sigma} \approx 0$ remain in equilibrium and the anomalous transition would not be observed. (ii) If $\Gamma_A \ll \Gamma \ll \Gamma_h$, a nontrivial steady state Andreev population $n_{A,\sigma} \neq 0, 1$ can form, so both transition types will be observed so long as both resonances ν_{\pm} are pumped. (iii) If $\Gamma_h \ll \Gamma$, steady state absorption is limited by the paucity of absorbing valence electrons. Instead re-emission, not captured in Eq. (6), will drive Rabi-like oscillation of electrons between the conduction and valence bands. Nevertheless, normal and anomalous transitions involve valence electrons of opposite spin so anomalous transitions can still take place.

Example geometry.—We illustrate the Andreev absorption spectrum in a representative junction geometry. We empha-

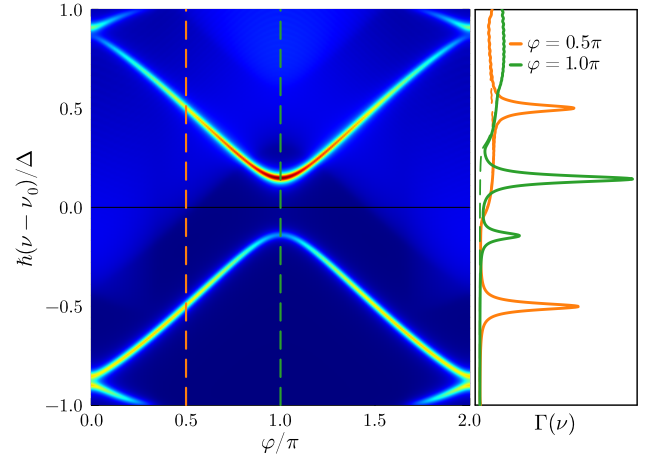


FIG. 2. Absorption spectrum versus junction phase φ . Junction parameters are given in the text. $\hbar\nu_0 = E_0 + E_F$ is the transition frequency from the trapped valence state to the Fermi energy. The right panel shows line cuts at $\varphi/\pi = 1/2, 1$. The dashed curves indicate the contribution of the valence band continuum edge.

size that the model we present here is quite general, but for concreteness we consider parameter values relevant to aluminum-proximitized indium arsenide (Al-InAs) [52, 53]. We take typical values $\Delta = 0.1$ meV and $E_F = 1.2$ meV. The corresponding Fermi momentum is $k_F^{-1} \sim 35$ nm. We take a moderately long junction length $L = 470$ nm as a practical target for delivering light with a small-bore aperture, near-field tip, or optical fiber waveguide. Nevertheless, for these parameters the coherence length $\xi = \hbar v_F / 2\Delta \sim 400$ nm, so the junction is effectively short and there is only one subgap Andreev level that persists for all φ .

Junctions typically have only partial transparency which we model with a potential barrier $V(x) = V_0 \delta(x - L_Z)$. Alternatively, a trapping potential can be imposed with electrostatic gates. We take a weak dimensionless barrier strength [4, 54] $Z = V_0 k_F / 2E_F = 0.2$ (corresponding $V_0 \approx 16.7$ meVnm), giving transparency $\tau = 1/(1 + Z^2) \approx 0.96$. We displace the barrier from the junction center, taking $L_Z = L/4$, to avoid a fine-tuned inversion symmetry, see below. Holes feel an inverted potential $-V(x)$, so the barrier naturally produces the discrete valence orbital we require, at binding energy $\approx 0.47\Delta$ above the valence band continuum. In this model the holes are absolutely bound ($\Gamma_h = 0$), and we broaden them to $\Gamma_h = 0.02\Delta$ ($2\pi/\Gamma_h \sim 2$ ns) for visual discernibility.

We plot the absorption rate $\Gamma(\nu)$ of Eq. (6) in Fig. 2. At each φ we obtain E_A and $\mathcal{D}_{e,h}$ from exactly diagonalizing the BdG Hamiltonian [Appendix]. To display both normal and anomalous transitions, we take $n_{A,\sigma} = 0.5$ and $n_{h,\sigma} = 1$. Here $\hbar\nu_0 = E_0 + E_F$ (≈ 420 meV in InAs), and includes the hole binding energy. The convex and concave curves correspond to the normal and anomalous transitions, respectively. The relative prominence of each transition is controlled by the matrix elements $\mathcal{D}_{e,h}(\varphi)$ which disperse with phase. At $\varphi = \pi$, $D_h \ll D_e$. This is a vestige of the inversion symmetry we broke by hand; an even $V(x)$ leads to definite-parity wavefunctions and

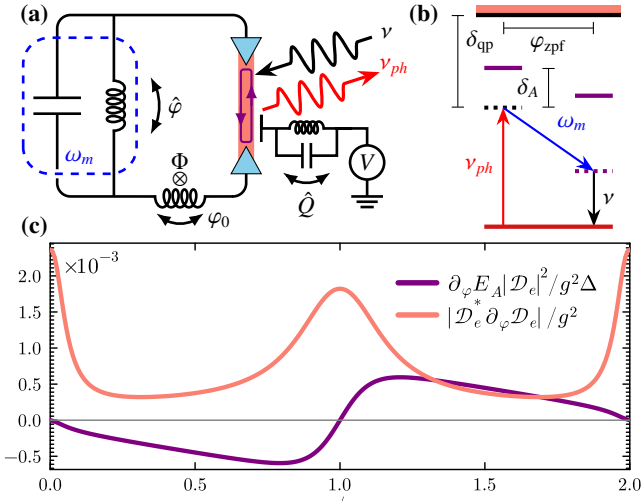


FIG. 3. Andreev optical-to-microwave transduction. (a) Circuit electrodynamics diagram. The SNS junction (cyan/pink/cyan) is embedded in an electromagnetic environment with equivalent circuit representation. The junction phase is set by an external bias φ_0 and further modulated by the phase fluctuations $\hat{\varphi}$ of a microwave resonance ω_m (blue). A classical idler beam (black) provides the energy to convert microwave photons to optical photons (red) and vice versa. An electrostatic side gate tunes the semiconductor doping and/or valence impurity state; the ABS also couples to microwave gate charge fluctuations \hat{Q} , not pursued in this work. (b) Schematic level diagram. A detuned optical photon ν_{ph} (red) excites the junction into a virtual state (dashed black). This could be the Andreev level (purple, detuning δ_A) or other quasiparticle states, like the above-gap continuum (cyan, detuning δ_{qp}). Emitting a microwave photon (blue) to the environment modulates the junction phase by $\sim \varphi_{zpf}$. Since the ABS energy and wavefunction depend on phase, this scatters the virtual state to the new Andreev level. If δ_{qp} is large, the quasiparticle-mediated transitions are captured in a renormalized dipole element $\mathcal{D}_e + \partial_\varphi \mathcal{D}_e \hat{\varphi}$. Finally, the idler drive (black) de-excites the ABS. (c) Transduction amplitudes for transitions via a virtual ABS (purple) or the other quasiparticle states (pink), corresponding to the numerators in Eq. (8). Note that the former, $\propto \partial_\varphi E_A$, enters Eq. (8) augmented by a factor $\sim \Delta/\hbar\omega_m \gg 1$. Same device parameters as Fig. 2.

associated selection rules that imply $D_h(\varphi = \pi) = 0$ [see Appendix]. Similar interference effects can suppress the transitions at high-symmetry $\varphi = 0, \pi$ or fine-tuned $k_F L$ and $k_F L_Z$ products. We illustrate other parameter combinations in the Appendix.

The ABS spectrum deviates from the usual formula [55] $E_A^2 = \Delta^2[1 - \tau \sin^2(\varphi/2)]$ due to the relatively large values of Δ/E_F and L/ξ . The latter also produces a high-energy ABS at the gap periphery near $\varphi = 0$. As φ increases, the higher ABS merges into the (unbound) quasiparticle continuum, and its transition dipoles continuously tend to zero since the light-matter interaction (3) is restricted to the normal region. Similarly, transitions originating from delocalized valence band continuum states also have only small transition dipole matrix elements. They thus make an additional weak contribution to the absorption spectrum, appearing as the faint chevron in Fig. 2. The side panel shows line cuts at $\varphi = \pi/2, \pi$, where the contribution of the continuum is marked with dashed curves.

Microwave transduction.—Once the optical coupling of the Andreev states has been characterized by absorption spectroscopy, it can be put to work. So far the ABS wavefunctions depended implicitly on the junction phase φ . If the junction is embedded in a superconducting circuit, the microwave-range dynamics of φ will couple to the ABSs. This forms the basis for microwave spectroscopy and gate operation in Andreev qubits [8, 9, 11–15, 18, 56–60]. Consequently, we propose that the Andreev levels can mediate interactions between microwave and optical photons, namely realizing a coherent microwave–optical photon transducer.

We sketch the circuit model in Fig. 3a. The phase-dependent circuit ground state energy (to which the ABSs contribute) is least for some φ_0 that is determined by an external flux bias. Promoting the phase variable to a quantum operator $\varphi \mapsto \varphi_0 + \hat{\varphi}$ and expanding in the quantum fluctuations yields the circuit mode $\hat{\varphi} = \varphi_{zpf}(\hat{b}^\dagger + \hat{b})$ at microwave frequency ω_m which may depend on φ_0 . φ_{zpf} is the mode zero-point phase fluctuations, typically $\ll 2\pi$ for low-impedance circuits. Its smallness allows us to linearize Hamiltonian (1) in $\hat{\varphi}$ [8]. Furthermore, by replacing $\alpha e^{-i\varphi} \mapsto \alpha e^{-i\varphi} + \hat{a}$ we introduce a quantized optical mode \hat{a} , with frequency ν_{ph} . ν , known in this context as the idler tone, provides the energy to convert microwave photons to the optical, and thus must be tuned to $\nu = \nu_{ph} - \omega_m$. In the frame rotating with the idler, the linearized Hamiltonian is

$$\hat{H} \simeq \sum_{\sigma} (E_A + \partial_\varphi E_A \hat{\varphi}) \hat{\gamma}_{\sigma}^{\dagger} \hat{\gamma}_{\sigma} + \sum_{\sigma} (\mathcal{D}_e + \partial_\varphi \mathcal{D}_e \hat{\varphi}) (\alpha + \hat{a}) \hat{\gamma}_{\sigma}^{\dagger} \hat{h}_{\sigma} + \text{H. c.} + \sum_{\sigma} (E_0 + E_F - \hbar\nu) \hat{h}_{\sigma}^{\dagger} \hat{h}_{\sigma} + \hbar(\nu_{ph} - \nu) \hat{a}^{\dagger} \hat{a} + \hbar\omega_m \hat{b}^{\dagger} \hat{b}. \quad (7)$$

Hereafter the φ_0 dependence of E_A , \mathcal{D}_e and ω_m is suppressed. While Eq. (7) seems like a trivial differentiation of Eq. (1), this Hamiltonian [derived in the Appendix] arises after eliminating higher quasiparticle states, and takes its current form only in a specific gauge and under certain conditions. Namely, we assumed that E_A is isolated from other quasiparticle states (including additional ABSs), and that the optical mode detuning from the Andreev level satisfies $|\mathcal{D}_e| \ll |\hbar\nu - E_0 - E_F - E_A| \ll \Delta$ so that the ABS is excited only virtually while the coupling to higher states is perturbatively smaller, respectively. The former condition allows us in this section to dispense with the anomalous transition terms in Eq. (4). Assuming $\omega_m \ll E_A$ allowed us to adiabatically eliminate parity-conserving two-ABS microwave drive terms $\sim \hat{\varphi} \hat{\gamma}_{\uparrow}^{\dagger} \hat{\gamma}_{\downarrow}^{\dagger}$. Eliminating the higher states may produce an AC Stark shift of the ABS which we absorb into E_A . Note the foregoing assumptions require that either φ_0 is not too close to $0, \pi$, or that the junction transparency is sufficiently below unity.

Virtual transitions into the Andreev states mediate interactions between the photons. Integrating out the fermions in Eq. (7) and focusing on photon-conserving terms, we obtain the transduction term $\hat{H}_{\text{eff}} = \hbar\Omega \hat{b}^{\dagger} \hat{a} + \text{H. c.} + \dots$ with the transduction Rabi coupling

$$\frac{\hbar\Omega}{2\alpha^* \varphi_{zpf}} = \frac{|\mathcal{D}_e|^2 (\partial_\varphi E_A)/\hbar}{(\nu - \nu_A)(\nu_{ph} - \nu_A)} + \frac{(\partial_\varphi \mathcal{D}_e^*) \mathcal{D}_e}{\nu_{ph} - \nu_A} + \frac{\mathcal{D}_e^* (\partial_\varphi \mathcal{D}_e)}{\nu - \nu_A} \quad (8)$$

where we introduced the notation $\nu_A = (E_0 + E_F + E_A)/\hbar$.

The processes contributing to Ω are schematically illustrated in Fig. 3b and can be understood as follows: The first term in Eq. (8) arises at third order and represents the sequence (i) absorption of an optical photon virtually excites the ABS, (ii) emission of a microwave photon by the parametric coupling $\hat{\phi}\hat{\gamma}^\dagger\hat{\gamma}$, and (iii) an idler-induced de-excitation of the ABS. The other two terms arise due to the four-way interaction $\hat{\phi}\hat{\alpha}\hat{\gamma}^\dagger\hat{h}$ in the renormalized dipole moment. Their microscopic origin is in similar sequences which initially excite other quasiparticle states rather than the ABS directly. Summing over all quasiparticle states gives rise to the $\partial_\varphi\mathcal{D}_e$ term in Eq. (7) [Appendix]. Virtual excitations of two ABSs by a microwave photon [11] (not drawn) also contribute.

We plot the amplitude of these two pathways versus phase bias in Fig. 3c. We estimate their relative strengths by $\sim |\mathcal{D}_e|^2 E_A/2\pi\hbar\omega_m$ and $\sim \partial_\varphi|\mathcal{D}_e|^2 \sim |\mathcal{D}_e|^2/2\pi$. Therefore, all else being equal, we expect the first term to be parametrically stronger by $\sim E_A/\hbar\omega_m \gg 1$ and dominate at generic phases [see e.g. at $\varphi_0 = 3\pi/2$]. Conversely, $\partial_\varphi E_A = 0$ at the high-symmetry points $\varphi_0 = 0, \pi$. $\mathcal{D}_e(\varphi)$ has a complex phase that winds rapidly, giving large $\partial_\varphi\mathcal{D}_e \neq 0$ peaks at these points. Altogether, this allows transduction at all bias points φ_0 .

The scale of Fig. 3c is controlled by $|\mathcal{D}_e|$, $\approx 0.055g$ at $\varphi = \pi$ for the parameters used here. The comparatively small overlap between the ABS and valence orbital can be understood as interband momentum mismatch, since Eq. (5) essentially sieves the k_F component of $f(x)$. The latter has bandwidth $\sim m_v V_0/\hbar^2$. Here we assumed for simplicity equal band masses $m_v = m_c$, yet group III–V semiconductors like InAs also host heavy valence holes with $m_v/m_c \sim 16$ [61, see also Appendix]. We verified numerically that a modest doubling of the valence mass and barrier height (transparency 0.86) boost $|\mathcal{D}_e|^2$ by a factor $\gtrsim 12$. Due to this relative sensitivity to details of the geometry and optical coupling, we refrain from estimating the total transduction efficiency.

In the foregoing treatment we assumed that both the idler and optical mode are closely tuned to the same ABS level E_A . Another scheme that could increase Ω can be devised if say the idler is tuned close to another ABS at some E_B , thus transducing $\omega_m \approx |E_B - E_A|$. However, in that case \hat{H} will not take the compact form in Eq. (7). Additionally, this seems less practical as fabrication of junctions of length $\gtrsim \xi$ is challenging, and the resulting large microwave frequency may be outside experimental setup bandwidths. Lastly, microwaves can also be coupled in by charge fluctuations in the electrostatic gate [12, 58, cf. Fig. 3a]. This will appear as a modulated potential $V(x) \rightarrow V(x) + \partial_Q V(x) i Q_{\text{zpf}} (\hat{b}^\dagger - \hat{b})$, where Q_{zpf} is the zero-point charge fluctuations; the doping level E_F will also

be affected. Interestingly, microwaves will now also couple to the valence state. Nevertheless, Q_{zpf} is typically $\gg 1$ if the circuit impedance is small, so may provide a stronger transduction mechanism. We defer these directions to future work.

Conclusions.—In this manuscript we presented a minimal model that couples Andreev bound states to optical-range light. We found two novel processes that emerge from this mechanism: First, a spectrally distinct “anomalous” optical absorption into occupied ABSs. This resonance counteracts junction saturation, allowing continuous absorption of bichromatic light. Second, that Andreev bound states can mediate transduction between optical and microwave photons.

While the strong coupling of ABSs to microwaves is well established, the strength of the optical coupling is somewhat sensitive due to the wavefunction overlap that determines the matrix elements $\mathcal{D}_{e,h}$. A more consistent hole wavefunction may be obtained by chemically *p*-doping the semiconductor with acceptor states. Furthermore, the optical response of semiconductors is dominated by exciton resonances, as the tight binding of the electron and hole greatly enhances the oscillator strength and separates it from band-edge transitions. This leaves room for an improved theory that incorporates electron–hole interactions that are consistent with the induced superconductivity and likely strong screening.

The coupling we describe here raises several intriguing prospects under the umbrella of “Andreev optoelectronics”: Optical driving can be pulsed so that a myriad of time-resolved experiments can be designed. Ultrafast pumps may permit the internal dynamics of the junction to be filmed in time. The ABSs carry the Josephson current, begging the question of whether transport through the junction can be tuned with optical illumination as it can be with microwave irradiation [62]. A first step would involve measuring the junction “photocurrent” due to the excitation of the Andreev states. Notably, optical injection may also present a controlled method of resetting the parity of Andreev quantum dots, which can then be determined by measuring optical transmission and reflection at the anomalous absorption frequency. Moreover, optically injected electrons may also effectively implement a third terminal or shed light on the elusive superconducting field effect [63]. Finally, beyond interfacing with microwave circuitry, the optical coupling we describe here may open a path to the readout and control of quantum information stored directly in the Andreev levels.

Acknowledgments.—We thank V. Fatemi, J. Shabani, K. Sardashti and A. Yacobi, for insightful discussions. J.S. acknowledges support from the Joint Quantum Institute and the Laboratory of Physical Sciences through the Condensed matter theory center. P.G. acknowledges support from NSF DMR 2315063 and 2130544.

-
- [1] A. F. Andreev, The thermal conductivity of the intermediate state in superconductors, *Sov. Phys. JETP* **19**, 1228 (1964).
 - [2] A. F. Andreev, Electron spectrum of the intermediate state of superconductors, *Sov. Phys. JETP* **22**, 455 (1966).
 - [3] I. O. Kulik, Macroscopic Quantization and the Proximity Effect

- in S-N-S Junctions, *Zh. Eksp. Teor. Fiz.* **57**, 1745 (1969).
- [4] P. F. Bagwell, Suppression of the Josephson current through a narrow, mesoscopic, semiconductor channel by a single impurity, *Phys. Rev. B* **46**, 12573 (1992).
- [5] N. M. Chtchelkatchev and Yu. V. Nazarov, Andreev Quan-

- tum Dots for Spin Manipulation, *Phys. Rev. Lett.* **90**, 226806 (2003).
- [6] M. Hays, V. Fatemi, D. Bouman, J. Cerrillo, S. Diamond, K. Serniak, T. Connolly, P. Krogstrup, J. Nygård, A. Levy Yeyati, A. Geresdi, and M. H. Devoret, Coherent manipulation of an Andreev spin qubit, *Science* **373**, 430 (2021).
- [7] H. Lu, Andreev spin relaxation time in a shadow-evaporated InAs weak link, *Phys. Rev. Appl.* **24**, 10.1103/v3lq-t5z8 (2025).
- [8] A. Zazunov, V. S. Shumeiko, E. N. Bratus', J. Lantz, and G. Wendin, Andreev Level Qubit, *Phys. Rev. Lett.* **90**, 087003 (2003).
- [9] L. Y. Cheung, R. Haller, A. Kononov, C. Ciaccia, J. H. Ungerer, T. Kanne, J. Nygård, P. Winkel, T. Reisinger, I. M. Pop, A. Baumgartner, and C. Schönenberger, Photon-mediated long-range coupling of two Andreev pair qubits, *Nat. Phys.* **20**, 1793 (2024).
- [10] R. M. Lutchyn, Majorana Fermions and a Topological Phase Transition in Semiconductor-Superconductor Heterostructures, *Phys. Rev. Lett.* **105**, 10.1103/PhysRevLett.105.077001 (2010).
- [11] L. Bretheau, Ç. Ö. Girit, H. Pothier, D. Esteve, and C. Urbina, Exciting Andreev pairs in a superconducting atomic contact, *Nature* **499**, 312 (2013).
- [12] L. Tosi, C. Metzger, M. F. Goffman, C. Urbina, H. Pothier, S. Park, A. L. Yeyati, J. Nygard, and P. Krogstrup, Spin-Orbit Splitting of Andreev States Revealed by Microwave Spectroscopy, *Phys. Rev. X* **9**, 011010 (2019).
- [13] F. J. Matute-Canadas, C. Metzger, S. Park, L. Tosi, P. Krogstrup, J. Nygard, M. F. Goffman, C. Urbina, H. Pothier, and A. L. Yeyati, Signatures of Interactions in the Andreev Spectrum of Nanowire Josephson Junctions, *Phys. Rev. Lett.* **128**, 197702 (2022).
- [14] M. Hinderling, S. C. ten Kate, M. Coraiola, D. Haxell, M. Stiefel, M. Mergenthaler, S. Paredes, S. Bedell, D. Sabonis, and F. Nichele, Direct Microwave Spectroscopy of Andreev Bound States in Planar Ge Josephson Junctions, *PRX Quantum* **5**, 030357 (2024).
- [15] B. H. Elfeky, K. Dindial, D. S. Brandão, B. Pekerten, J. Lee, W. M. Strickland, P. J. Strohhoben, A. Danilenko, L. Baker, M. Mikalsen, W. Schiela, Z. Liang, J. Issokson, I. Levy, I. Žutić, and J. Shabani, Microwave Andreev bound state spectroscopy in a semiconductor-based Planar Josephson junction, *Phys. Rev. Research* **7**, 013248 (2025).
- [16] T. W. Larsen, Semiconductor-Nanowire-Based Superconducting Qubit, *Phys. Rev. Lett.* **115**, 10.1103/PhysRevLett.115.127001 (2015).
- [17] L. Casparis, M. R. Connolly, M. Kjaergaard, N. J. Pearson, A. Kringhøj, T. W. Larsen, F. Kuemmeth, T. Wang, C. Thomas, S. Gronin, G. C. Gardner, M. J. Manfra, C. M. Marcus, and K. D. Petersson, Superconducting gatemon qubit based on a proximitized two-dimensional electron gas, *Nature Nanotech* **13**, 915 (2018).
- [18] G. de Lange, Realization of Microwave Quantum Circuits Using Hybrid Superconducting-Semiconducting Nanowire Josephson Elements, *Phys. Rev. Lett.* **115**, 10.1103/PhysRevLett.115.127002 (2015).
- [19] A. Hertel, Gate-Tunable Transmon Using Selective-Area-Grown Superconductor-Semiconductor Hybrid Structures on Silicon, *Phys. Rev. Appl.* **18**, 10.1103/PhysRevApplied.18.034042 (2022).
- [20] B. H. Elfeky, W. M. Strickland, J. Lee, J. T. Farmer, S. Shanto, A. Zarassi, D. Langone, M. G. Vavilov, E. M. Levenson-Falk, and J. Shabani, Quasiparticle Dynamics in Epitaxial Al/InAs Planar Josephson Junctions, *PRX Quantum* **4**, 030339 (2023).
- [21] O. Sagi, A. Crippa, M. Valentini, M. Janik, L. Baghumyan, G. Fabris, L. Kapoor, F. Hassani, J. Fink, S. Calcaterra, D. Chrastina, G. Isella, and G. Katsaros, A gate tunable transmon qubit in planar Ge, *Nat Commun* **15**, 6400 (2024).
- [22] H. Zheng, L. Y. Cheung, N. Sangwan, A. Kononov, R. Haller, J. Ridderbos, C. Ciaccia, J. H. Ungerer, A. Li, E. P. Bakkers, A. Baumgartner, and C. Schönenberger, Coherent Control of a Few-Channel Hole Type Gatemon Qubit, *Nano Lett.* **24**, 7173 (2024).
- [23] E. Kiyooka, C. Tangchingchai, L. Noirot, A. Leblanc, B. Brun, S. Zihlmann, R. Maurand, V. Schmitt, É. Dumur, J.-M. Hartmann, F. Lefloch, and S. De Franceschi, Gatemon Qubit on a Germanium Quantum-Well Heterostructure, *Nano Lett.* **25**, 562 (2025).
- [24] C. T. Ke, C. M. Moehle, F. K. de Vries, C. Thomas, S. Metti, C. R. Guinn, R. Kallaher, M. Lodari, G. Scappucci, T. Wang, R. E. Diaz, G. C. Gardner, M. J. Manfra, and S. Goswami, Ballistic superconductivity and tunable π -junctions in InSb quantum wells, *Nat Commun* **10**, 3764 (2019).
- [25] S. A. Khan, C. Lampadaris, A. Cui, L. Stampfer, Y. Liu, S. J. Pauka, M. E. Cachaza, E. M. Fiordaliso, J.-H. Kang, S. Korneychuk, T. Mutas, J. E. Sestoft, F. Krizek, R. Tanta, M. C. Cassidy, T. S. Jespersen, and P. Krogstrup, Highly Transparent Gateable Superconducting Shadow Junctions, *ACS Nano* **14**, 14605 (2020).
- [26] V. Levajac, J.-Y. Wang, C. Sfiligoj, M. Lemang, J. C. Wolff, A. Bordin, G. Badawy, S. Gazibegovic, E. P. A. M. Bakkers, and L. P. Kouwenhoven, Subgap spectroscopy along hybrid nanowires by nm-thick tunnel barriers, *Nat Commun* **14**, 6647 (2023).
- [27] G. Nanda, J. L. Aguilera-Servin, P. Rakyta, A. Kormányos, R. Kleiner, D. Koelle, K. Watanabe, T. Taniguchi, L. M. K. Vandersypen, and S. Goswami, Current-Phase Relation of Ballistic Graphene Josephson Junctions, *Nano Lett.* **17**, 3396 (2017).
- [28] J. I.-J. Wang, D. Rodan-Legrain, L. Bretheau, D. L. Campbell, B. Kannan, D. Kim, M. Kjaergaard, P. Krantz, G. O. Samach, F. Yan, J. L. Yoder, K. Watanabe, T. Taniguchi, T. P. Orlando, S. Gustavsson, P. Jarillo-Herrero, and W. D. Oliver, Coherent control of a hybrid superconducting circuit made with graphene-based van der Waals heterostructures, *Nature Nanotech* **14**, 120 (2019).
- [29] H. Riechert, S. Annabi, A. Peugeot, H. Duprez, M. Hantute, K. Watanabe, T. Taniguchi, E. Arrighi, J. Griesmar, J.-D. Pillet, and L. Bretheau, The carbon nanotube gatemon qubit, *Nat Commun* **16**, 7197 (2025).
- [30] K.-H. Lee, S. Chakram, S. E. Kim, F. Mujid, A. Ray, H. Gao, C. Park, Y. Zhong, D. A. Muller, D. I. Schuster, and J. Park, Two-Dimensional Material Tunnel Barrier for Josephson Junctions and Superconducting Qubits, *Nano Lett.* **19**, 8287 (2019).
- [31] J. Balgley, Crystalline superconductor-semiconductor Josephson junctions for compact superconducting qubits, *Phys. Rev. Appl.* **24**, 10.1103/3ssz-jjt6 (2025).
- [32] M. J. Weaver, P. Duivesteyn, A. C. Bernasconi, S. Scharmer, M. Lemang, T. C. van Thiel, F. Hijazi, B. Hensen, S. Gröblacher, and R. Stockill, An integrated microwave-to-optics interface for scalable quantum computing, *Nat. Nanotechnol.* **19**, 166 (2024).
- [33] H. K. Warner, J. Holzgrafe, B. Yankelevich, D. Barton, S. Polletto, C. J. Xin, N. Sinclair, D. Zhu, E. Sete, B. Langley, E. Batson, M. Colangelo, A. Shams-Ansari, G. Joe, K. K. Berggren, L. Jiang, M. J. Reagor, and M. Lončar, Coherent control of a superconducting qubit using light, *Nat. Phys.* **21**, 831 (2025).
- [34] G. Arnold, T. Werner, R. Sahu, L. N. Kapoor, L. Qiu, and J. M. Fink, All-optical superconducting qubit readout, *Nat. Phys.* **21**,

- 393 (2025).
- [35] T. C. van Thiel, M. J. Weaver, F. Berto, P. Duivestijn, M. Lemang, K. L. Schuurman, M. Žemlička, F. Hijazi, A. C. Bernasconi, C. Ferrer, E. Cataldo, E. Lachman, M. Field, Y. Mohan, F. K. de Vries, C. C. Bultink, J. C. van Oven, J. Y. Mutus, R. Stockill, and S. Gröblacher, Optical readout of a superconducting qubit using a piezo-optomechanical transducer, *Nat. Phys.* **21**, 401 (2025).
 - [36] J. Bochmann, A. Vainsencher, D. D. Awschalom, and A. N. Cleland, Nanomechanical coupling between microwave and optical photons, *Nature Phys* **9**, 712 (2013).
 - [37] R. W. Andrews, R. W. Peterson, T. P. Purdy, K. Cicak, R. W. Simmonds, C. A. Regal, and K. W. Lehnert, Bidirectional and efficient conversion between microwave and optical light, *Nature Phys* **10**, 321 (2014).
 - [38] A. Rueda, F. Sedlmeir, M. C. Collodo, U. Vogl, B. Stiller, G. Schunk, D. V. Strekalov, C. Marquardt, J. M. Fink, O. Painter, G. Leuchs, and H. G. L. Schwefel, Efficient microwave to optical photon conversion: An electro-optical realization, *Optica*, *OPTICA* **3**, 597 (2016).
 - [39] W. Jiang, C. J. Sarabalis, Y. D. Dahmani, R. N. Patel, F. M. Mayor, T. P. McKenna, R. Van Laer, and A. H. Safavi-Naeini, Efficient bidirectional piezo-optomechanical transduction between microwave and optical frequency, *Nat Commun* **11**, 1166 (2020).
 - [40] M. Mirhosseini, A. Sipahigil, M. Kalaei, and O. Painter, Superconducting qubit to optical photon transduction, *Nature* **588**, 599 (2020).
 - [41] M. Wu, E. Zeuthen, K. C. Balram, and K. Srinivasan, Microwave-to-Optical Transduction Using a Mechanical Supermode for Coupling Piezoelectric and Optomechanical Resonators, *Phys. Rev. Appl.* **13**, 014027 (2020).
 - [42] N. J. Lambert, A. Rueda, F. Sedlmeir, and H. G. L. Schwefel, Coherent Conversion Between Microwave and Optical Photons—An Overview of Physical Implementations, *Advanced Quantum Technologies* **3**, 1900077 (2020).
 - [43] X. Han, W. Fu, C.-L. Zou, L. Jiang, and H. X. Tang, Microwave-optical quantum frequency conversion, *Optica*, *OPTICA* **8**, 1050 (2021).
 - [44] H. Le Sueur, P. Joyez, H. Pothier, C. Urbina, and D. Esteve, Phase Controlled Superconducting Proximity Effect Probed by Tunneling Spectroscopy, *Phys. Rev. Lett.* **100**, 197002 (2008).
 - [45] J.-D. Pillet, C. H. L. Quay, P. Morfin, C. Bena, A. L. Yeyati, and P. Joyez, Andreev bound states in supercurrent-carrying carbon nanotubes revealed, *Nature Phys* **6**, 965 (2010).
 - [46] M. Meschke, J. T. Pelttonen, J. P. Pekola, and F. Giazotto, Tunnel spectroscopy of a proximity Josephson junction, *Phys. Rev. B* **84**, 214514 (2011).
 - [47] L. Bretheau, J. I.-J. Wang, R. Pisoni, K. Watanabe, T. Taniguchi, and P. Jarillo-Herrero, Tunneling spectroscopy of Andreev states in graphene, *Nature Phys* **13**, 756 (2017).
 - [48] I. Martin and D. Mozyrsky, Nonequilibrium theory of tunneling into a localized state in a superconductor, *Phys. Rev. B* **90**, 100508 (2014).
 - [49] F. Setiawan and J. D. Sau, Electron-boson-interaction induced particle-hole symmetry breaking of conductance into subgap states in superconductors, *Phys. Rev. Res.* **3**, L032038 (2021).
 - [50] A. Yazdani, B. A. Jones, C. P. Lutz, M. F. Crommie, and D. M. Eigler, Probing the Local Effects of Magnetic Impurities on Superconductivity, *Science* **275**, 1767 (1997).
 - [51] M. Ruby, F. Pientka, Y. Peng, F. von Oppen, B. W. Heinrich, and K. J. Franke, Tunneling Processes into Localized Subgap States in Superconductors, *Phys. Rev. Lett.* **115**, 087001 (2015).
 - [52] R. Aguado, A perspective on semiconductor-based superconducting qubits, *Appl. Phys. Lett.* **117**, 10.1063/5.0024124 (2020).
 - [53] G. Badawy and E. P. A. M. Bakkers, Electronic Transport and Quantum Phenomena in Nanowires, *Chem. Rev.* **124**, 2419 (2024).
 - [54] G. E. Blonder, M. Tinkham, and T. M. Klapwijk, Transition from metallic to tunneling regimes in superconducting microconstrictions: Excess current, charge imbalance, and supercurrent conversion, *Phys. Rev. B* **25**, 4515 (1982).
 - [55] C. W. J. Beenakker, Universal limit of critical-current fluctuations in mesoscopic Josephson junctions, *Phys. Rev. Lett.* **67**, 3836 (1991).
 - [56] M. Hays, G. de Lange, K. Serniak, D. J. van Woerkom, D. Bouman, P. Krogstrup, J. Nygård, A. Geresdi, and M. H. Devoret, Direct Microwave Measurement of Andreev-Bound-State Dynamics in a Semiconductor-Nanowire Josephson Junction, *Phys. Rev. Lett.* **121**, 047001 (2018).
 - [57] C. Janvier, L. Tosi, L. Bretheau, Ç. Ö. Girit, M. Stern, P. Bertet, P. Joyez, D. Vion, D. Esteve, M. F. Goffman, H. Pothier, and C. Urbina, Coherent manipulation of Andreev states in superconducting atomic contacts, *Science* **349**, 1199 (2015).
 - [58] C. Metzger, S. Park, L. Tosi, C. Janvier, A. A. Reynoso, M. F. Goffman, C. Urbina, A. Levy Yeyati, and H. Pothier, Circuit-QED with phase-biased Josephson weak links, *Phys. Rev. Res.* **3**, 013036 (2021).
 - [59] D. J. van Woerkom, A. Proutski, B. van Heck, D. Bouman, J. I. Väyrynen, L. I. Glazman, P. Krogstrup, J. Nygård, L. P. Kouwenhoven, and A. Geresdi, Microwave spectroscopy of spinful Andreev bound states in ballistic semiconductor Josephson junctions, *Nature Phys* **13**, 876 (2017).
 - [60] J. J. Wesdorp, F. J. Matute-Canadas, A. Vaartjes, L. Grünhaupt, T. Laeven, S. Roelofs, L. J. Splitthoff, M. Pita-Vidal, A. Bargerbos, D. J. van Woerkom, P. Krogstrup, L. P. Kouwenhoven, C. K. Andersen, A. L. Yeyati, B. van Heck, and G. de Lange, Microwave spectroscopy of interacting Andreev spins, *Phys. Rev. B* **109**, 045302 (2024).
 - [61] I. Vurgaftman, J. R. Meyer, and L. R. Ram-Mohan, Band parameters for III–V compound semiconductors and their alloys, *J. Appl. Phys.* **89**, 5815 (2001).
 - [62] D. Z. Haxell, M. Coraiola, D. Sabonis, M. Hinderling, S. C. ten Kate, E. Cheah, F. Krizek, R. Schott, W. Wegscheider, W. Belzig, J. C. Cuevas, and F. Nichele, Microwave-induced conductance replicas in hybrid Josephson junctions without Floquet—Andreev states, *Nat Commun* **14**, 6798 (2023).
 - [63] I. Golokolenov, A. Guthrie, S. Kafanov, Y. A. Pashkin, and V. Tsepelin, On the origin of the controversial electrostatic field effect in superconductors, *Nat Commun* **12**, 2747 (2021).

Appendix A: Microscopic model

In this section we describe the microscopic Hamiltonians for the valence and conduction bands.

In the conduction band we use a Bogoliubov–de-Gennes (BdG) mean-field Hamiltonian, usual for describing the SNS system [3, 4]. Assuming s -wave pairing and no spin–orbit coupling, the BdG Hamiltonian takes the form $\hat{H}_c = \int \hat{\Psi}^\dagger(x) \mathcal{H}_c(x) \hat{\Psi} dx$, where $\hat{\Psi} = [\hat{\psi}_{c\uparrow}, \hat{\psi}_{c\downarrow}^\dagger]^T$ is a Nambu particle–hole spinor in the conduction band, and the single-particle Hamiltonian density is the two-by-two differential operator

$$\mathcal{H}_c(x) = \begin{pmatrix} -\frac{\hbar^2}{2m_c} \partial_x^2 + V(x) - E_F & \Delta(x) \\ \Delta^*(x) & E_F + \frac{\hbar^2}{2m_c} \partial_x^2 - V(x) \end{pmatrix}. \quad (\text{A1})$$

Here E_F is the semiconductor Fermi level (measured from the bottom of the conduction band) and $V(x)$ is the electrostatic potential. \hat{H}_c will be diagonalized by BdG modes $\hat{\gamma}_\lambda^\dagger = \int [u_\lambda(x) \hat{\psi}_{c\uparrow}^\dagger(x) + v_\lambda(x) \hat{\psi}_{c\downarrow}(x)] dx$ with appropriate particle and hole amplitudes, $u_\lambda(x)$ and $v_\lambda(x)$, such that $[\hat{H}_c, \hat{\gamma}_\lambda^\dagger] = E_\lambda \hat{\gamma}_\lambda^\dagger$. Substituting this into \hat{H}_c , it can be shown that $[u_\lambda(x) \ v_\lambda(x)]^T$ are an eigenvector of the differential operator \mathcal{H}_c with eigenvalue E_λ .

Eq. (A1) has a particle–hole (p–h) anti-symmetry $\hat{\Theta} \mathcal{H}_c \hat{\Theta} = -\mathcal{H}_c$, where $\hat{\Theta} = -i\hat{\eta}_y \hat{\mathcal{K}}$, $\hat{\eta}_y$ is the second Pauli matrix acting in Nambu space, and $\hat{\mathcal{K}}$ is complex conjugation. Therefore, an eigenstate $[u_\lambda, v_\lambda]$ with eigenvalue E_λ has a symmetry partner with amplitudes $[-v_\lambda^*, u_\lambda^*]$ and energy $-E_\lambda$. Re-labeling $\hat{\gamma}_\lambda^\dagger \rightarrow \hat{\gamma}_\lambda$ for states with $E_\lambda < 0$, each state is now twice degenerate, which corresponds to the SU(2) spin symmetry of \hat{H} . This allows us to divide the index λ into orbital and particle–hole indices, $\lambda = (\alpha, \sigma)$, with α enumerating only the positive-energy eigenstates of \mathcal{H}_c and $\sigma = \uparrow, \downarrow$. With this separation we represent

$$\hat{H}_c = \sum_\lambda E_\lambda \hat{\gamma}_\lambda^\dagger \hat{\gamma}_\lambda = \sum_\alpha E_\alpha (\hat{\gamma}_{\alpha\uparrow}^\dagger \hat{\gamma}_{\alpha\uparrow} - \hat{\gamma}_{\alpha\downarrow} \hat{\gamma}_{\alpha\downarrow}^\dagger) \quad (\text{A2})$$

and inverse Bogoliubov transformation

$$\begin{pmatrix} \hat{\psi}_{c\uparrow}(x) \\ \hat{\psi}_{c\downarrow}^\dagger(x) \end{pmatrix} = \sum_\lambda \begin{pmatrix} u_\lambda(x) \\ v_\lambda(x) \end{pmatrix} \hat{\gamma}_\lambda = \sum_\alpha \begin{pmatrix} u_\alpha(x) \\ v_\alpha(x) \end{pmatrix} \hat{\gamma}_{\alpha\uparrow} + \begin{pmatrix} -v_\alpha^*(x) \\ u_\alpha^*(x) \end{pmatrix} \hat{\gamma}_{\alpha\downarrow}^\dagger. \quad (\text{A3})$$

In the main text we have restricted these to $\alpha = A$ with the lowest E_A , representing the one guaranteed Andreev bound state in the junction.

Now, the valence band Hamiltonian. We assume this band is sufficiently far from the Fermi surface such that any pairing correlations can be neglected, and take a normal Hamiltonian

$$\hat{H}_v = \sum_\sigma \psi_{v\sigma}(x) \mathcal{H}_v(x) \hat{\psi}_{v\sigma}(x) dx = \sum_\sigma \int \hat{\psi}_{v\sigma}^\dagger(x) \left[-\frac{\hbar^2}{2|m_v|} \partial_x^2 + V(x) - E_F - E_G \right] \hat{\psi}_{v\sigma}(x) dx = \sum_{n,\sigma} (E_n^{(v)} + E_F) \hat{h}_{n\sigma} \hat{h}_{n\sigma}^\dagger \quad (\text{A4})$$

where E_G is the optical bandgap between valence and conduction band extrema, and $|m_v| > 0$ is the inverted valence effective mass. The negative mass causes valence electrons to sense the inverted potential $-V(x)$. In the last expression we diagonalized this Hamiltonian in terms of valence states indexed by orbital n and spin σ . Similarly, in the main text we restricted this Hamiltonian to highest valence orbital (smallest $E_n^{(v)}$).

The junction geometry is determined by picking concrete $\Delta(x)$ and $V(x)$. For the superconducting order parameter $\Delta(x)$ we pick the phase convention

$$\Delta(x) = \begin{cases} \Delta e^{i\varphi/2}, & x > L/2 \\ 0, & |x| < L/2 \\ \Delta e^{-i\varphi/2}, & x < -L/2. \end{cases} \quad (\text{A5})$$

whereas for the electrostatic potential we take a single barrier $V_0 = V(x - L_Z)$, $|L_Z| < L/2$. For the special case that $L_Z = 0$, \hat{H} has a combined inversion–conjugation symmetry, see below.

To obtain Figs. 2 and 3b in the main text, we numerically diagonalize $\mathcal{H}_{c,v}$ by finite differences. The diagonalization volume includes the junction normal region ($|x| < L/2$) and additional 20,000 nm segments of the superconducting leads on either side. This large additional length is required for convergence of the ABSs which decay exponentially into the superconductors, as well as to capture the onset of the valence band continuum. We use open boundary conditions. To mitigate numerical noise, we smooth the step (delta) function in $\Delta(x)$ ($V(x)$) into a hyperbolic tangent (gaussian) with characteristic width 10 nm (1 nm), \ll the Fermi wavelength (~ 220 nm for the parameters used). Moreover, for simplicity we assume $|m_v| = m_c$, which is approximately

true for the light hole branch in group III-V semiconductors like InAs [61], and take $m_c = 0.024m_e$. This is the more stringent assumption: These semiconductors also have a heavy hole branch with $|m_v| \approx 16m_c$ [61]. Both the trap orbital's binding energy and inverse decay length are $\propto |m_v|$; therefore a massive hole will separate much more from the valence band continuum, and have momenta much closer to k_F , thereby increasing the wavefunction overlap in Eq. (5). Therefore the magnitudes $|\mathcal{D}_{e,h}|$ could be enhanced by an order of magnitude compared to those we present in the main text. We observed numerically that for the parameter values used in the main text, doubling the hole mass increases $|\mathcal{D}_e|^2$ by a factor ≈ 4 .

1. Selection rules at high symmetry

The combination of high-symmetry phase differences $\varphi = 0, \pi$ and a potential inversion symmetry $V(-x) = V(x)$ will result in additional selection rules that may preclude optical transitions (normal or anomalous) by fixing $\mathcal{D}_{e,h}$ to zero.

We first note that the exact subgap eigenstates of \hat{H} are not degenerate. This is natural for generic phase. At $\varphi = 0, \pi$, the ABS level crossing [3] is protected only by perfect junction transparency, and the crossing is split for generic normal scattering. An even $V(x)$ would lift the degeneracy at $\varphi = \pi$ but not necessarily at $\varphi = 0$ [4]. However, that result is derived within the Andreev approximation of no normal reflection at the SN boundaries [1–3], valid when $\Delta/E_F \rightarrow 0$. Any finite Δ will induce normal reflections that will lift the degeneracies at $\varphi = 0$ as well. Therefore, the exact eigenstates of \hat{H} are not degenerate and hence must be fixed by all symmetries of \hat{H} .

Now consider the additional symmetry at special values of φ . Namely, at $\varphi = 0$ (π) the term proportional to Δ in \mathcal{H}_c can be written $\Delta \eta_x [\Delta \text{sgn}(x) i \eta_y]$, showing that $i \eta_y$ (η_x) is a new antisymmetry. Combined with the p–h antisymmetry $i \eta_y \mathcal{K}$, it follows that \mathcal{K} and $\mathcal{K} \eta_z$ are symmetries for $\varphi = 0$ and $\varphi = \pi$, respectively.

Additionally, if the electrostatic potential $V(x)$ is even, \mathcal{H}_c has an inversion–conjugation symmetry \mathcal{PK} , with \mathcal{P} the inversion operation $x \rightarrow -x$, valid for all φ . Hence, at fine-tuned $\varphi = 0, \pi$ we have \mathcal{P} and $\mathcal{P} \eta_z$ as symmetries. That each ABS is not degenerate implies that $u(x)$ and $v(x)$ have the same (opposite) parity at $\varphi = 0$ (π). The valence Hamiltonian \mathcal{H}_v is also even and therefore the hole wavefunction $f(x)$ will also have definite parity (typically even). In total we conclude that at $\varphi = 0$ ABSs are characterized as having both $\mathcal{D}_e = \mathcal{D}_h = 0$ or both nonzero, while for $\varphi = \pi$, exactly one of the dipole elements vanishes.

Appendix B: Transduction matrix elements

In this section we derive the effective microwave transduction Hamiltonian. We slightly rewrite Eq.(A2), including the explicit phase dependence of both the quasiparticle energies and operators,

$$\hat{H}_c = \sum_{\alpha} E_{\alpha}(\varphi) \hat{\gamma}_{\alpha\sigma}^{\dagger}(\varphi) \hat{\gamma}_{\alpha\sigma}(\varphi) + E_J(\varphi) \quad (\text{B1})$$

The junction ground state is $E_J(\varphi) = -\sum_{\alpha} E_{\alpha}(\varphi) +$ any additional contributions from the microwave environment. It will be minimized at some φ_0 that can be tuned by an external flux bias. We obtain the microwave Hamiltonian by replacing $\varphi \mapsto \varphi_0 + \hat{\varphi}$ and linearizing in the fluctuation $\hat{\varphi}$ which we promote to a quantum operator [8]. Neglecting constants and higher nonlinearities, this yields $E_J(\varphi) = \hbar \omega_m \hat{b}^{\dagger} \hat{b}$, with \hat{b} the annihilation operator of a microwave photon at some frequency $\omega_m(\varphi_0)$, and $\hat{\varphi} = \varphi_{\text{zpf}}(\hat{b} + \hat{b}^{\dagger})$. Though the BdG Hamiltonian is highly nonlinear in φ , in low-impedance microwave circuits the zero-point fluctuations $\varphi_{\text{zpf}} \ll 2\pi$, allowing us nevertheless to linearize it in $\hat{\varphi}$. The phase dependence of the quasiparticle wavefunctions is lifted to the fermionic operators, which evolve with phase by

$$\frac{\partial \hat{\gamma}_{\alpha\uparrow}^{\dagger}}{\partial \varphi} = -i \sum_{\beta} [\hat{\gamma}_{\beta\uparrow}^{\dagger} \mathcal{A}_{\beta\alpha} + \hat{\gamma}_{\beta\downarrow} \mathcal{B}_{\beta\alpha}], \quad \frac{\partial \hat{\gamma}_{\alpha\downarrow}^{\dagger}}{\partial \varphi} = -i \sum_{\beta} [\hat{\gamma}_{\beta\downarrow}^{\dagger} \mathcal{A}_{\beta\alpha} - \hat{\gamma}_{\beta\uparrow} \mathcal{B}_{\beta\alpha}], \quad (\text{B2})$$

where the matrices \mathcal{A}, \mathcal{B} give the Andreev Berry connection

$$\mathcal{A}_{\beta\alpha} = i \int [u_{\beta}^*(x) \partial_{\varphi} u_{\alpha}(x) + v_{\beta}^*(x) \partial_{\varphi} v_{\alpha}(x)] dx, \quad \mathcal{B}_{\beta\alpha} = i \int [-v_{\beta}(x) \partial_{\varphi} u_{\alpha}(x) + u_{\beta}(x) \partial_{\varphi} v_{\alpha}(x)] dx, \quad (\text{B3})$$

with u, v evaluated at φ_0 . \mathcal{A}, \mathcal{B} are Hermitian and symmetric, respectively.

We now expand Eq. (B1) by the chain rule. We then add the valence band and light–matter coupling, which do not depend on phase so require no expansion. Moving to the rotating frame described in the main text, we have the Hamiltonian

$$\begin{aligned} \hat{H} = & \sum_{\alpha\sigma} E_{\alpha} \hat{\gamma}_{\alpha\sigma}^{\dagger} \hat{\gamma}_{\alpha\sigma} + \sum_{\alpha\beta\sigma} [\delta_{\alpha\beta} \partial_{\varphi} E_{\alpha} - i(E_{\alpha} - E_{\beta}) \mathcal{A}_{\beta\alpha}] \hat{\gamma}_{\beta\sigma}^{\dagger} \hat{\gamma}_{\alpha\sigma} \hat{\varphi} + [i(E_{\alpha} + E_{\beta}) \mathcal{B}_{\beta\alpha} \hat{\gamma}_{\beta\uparrow}^{\dagger} \hat{\gamma}_{\alpha\downarrow}^{\dagger} + \text{H. c.}] \hat{\varphi} + \hbar \omega_m \hat{b}^{\dagger} \hat{b} \\ & + \sum_{\sigma} (E_0 + E_F - \hbar v) \hat{h}_{\sigma} \hat{h}_{\sigma}^{\dagger} + \hbar(v_{ph} - v) \hat{a}^{\dagger} \hat{a} + \sum_{\alpha\sigma} [\mathcal{D}_e^{\alpha}(\varphi_0) \hat{\gamma}_{\alpha\sigma}^{\dagger} \hat{h}_{\sigma} + (-1)^{\sigma} \mathcal{D}_h^{\alpha}(\varphi_0) \hat{\gamma}_{\alpha\sigma} \hat{h}_{\sigma}^{\dagger}] (A + \hat{a}) + \text{H. c.} \end{aligned} \quad (\text{B4})$$

We suppress the argument φ_0 hereafter. In the last line we generalized Eqs. (4) and (5) to the entire quasiparticle spectrum, and defined $(-1)^{\uparrow,\downarrow} = \pm 1$. We reiterate that though the dipole matrix elements $D_{e,h}^\alpha(\varphi)$ disperse with phase, there is no $\propto \hat{\varphi}$ term in the light-matter interaction since the microscopic coupling [cf. Eq. (3)] does not depend on phase, $\partial_\varphi \hat{V} = 0$. The term $\propto \mathcal{B}^*$ is well-known as that allowing microwave-driven transitions in the parity-even sector of Andreev level qubits, see e.g. Ref. [11].

Our goal now is to integrate out high energy quasiparticle states to obtain an effective Hamiltonian for one Andreev level at index $\alpha = A$. For junction lengths $L \lesssim \xi$ and operating point φ_0 not too close to $0, \pi$, the Andreev levels are well-separated from each other and the continuum by energy of order $\sim \Delta$. The idler tone is tuned to energy conservation, so $\nu = \nu_{ph} - \omega_m$. We now assume the energy hierarchy

$$\mathcal{D}_e^A \ll |\nu_{ph} - E_0 - E_F - E_A| \ll \omega_m \ll E_A, \Delta \quad (\text{B5})$$

The first inequality implies the excitation of ABS A is perturbatively small. The last inequality implies excitations to quasiparticle states $\beta \neq A$ are parametrically weaker; this includes the double-excitation of the A ABS by the \mathcal{B} term. The middle inequality implies excitations of more than one photon, either a or b , is suppressed. Therefore, our low-energy manifold includes the ABS vacuum and at most one excitation in the A state. Note the latter assumption requires φ_0 not too close to π , or alternatively a transparency sufficiently below unity.

At lowest order, integrating out higher quasiparticle states will generate several kinds of terms: (i) a vacuum Stark shift renormalizing E_A , which we absorb into a redefinition of E_A ; (ii) four-wave mixing terms like $\sim \hat{\gamma}_A^\dagger \hat{\gamma}_A \hat{b}^{(\dagger)} \hat{b}^{(\dagger)}$ which will be weak perturbations by our assumption of large ω_m and small φ_{zpf} ; and (iii) a phase-dependent renormalization of \mathcal{D}_e^A . Focusing on the latter, we obtain the term

$$\begin{aligned} \hat{H}_{\text{eff}} &\ni \sum_{\beta \neq A} [-i(E_\beta - E_A) \mathcal{A}_{A\beta}] \hat{\gamma}_{A\sigma}^\dagger \hat{\varphi} \left(\frac{A \mathcal{D}_e^\beta}{\hbar\nu - (E_0 + E_F + E_\beta)} + \frac{\hat{a} \mathcal{D}_e^\beta}{\hbar\nu_{ph} - (E_0 + E_F + E_\beta)} \right) \hat{h}_\sigma \\ &\quad - \sum_{\beta} \mathcal{D}_h^\beta \hat{h}_\sigma \left(\frac{\hat{b}^\dagger}{-E_A - E_\beta - \omega_m} + \frac{\hat{b}}{-E_A - E_\beta + \omega_m} \right) \varphi_{zpf} [i(E_A + E_\beta) \mathcal{B}_{A\beta}^*] \hat{\gamma}_{A\sigma}^\dagger (A + \hat{a}) \\ &\approx \sum_{\beta \neq A} [i(E_\beta - E_A) \mathcal{A}_{A\beta}] \hat{\gamma}_{A\sigma}^\dagger \hat{\varphi} \left(\frac{(A + \hat{a}) \mathcal{D}_e^\beta}{E_A - E_\beta} \right) \hat{h}_\sigma + \sum_{\beta} \mathcal{D}_h^\beta \hat{h}_\sigma \left(\frac{(\hat{b} + \hat{b}^\dagger) \varphi_{zpf}}{E_A + E_\beta} \right) [i(E_A + E_\beta) \mathcal{B}_{A\beta}^*] \hat{\gamma}_{A\sigma}^\dagger (A + \hat{a}) \\ &= \hat{\gamma}_{A\sigma}^\dagger \hat{h}_\sigma \hat{\varphi} (A + \hat{a}) \left[i \sum_{\beta} (\mathcal{A}_{A\beta} \mathcal{D}_e^\beta - \mathcal{B}_{A\beta}^* \mathcal{D}_h^\beta) - i \mathcal{A}_{AA} \mathcal{D}_e^A \right] = \hat{\gamma}_{A\sigma}^\dagger \hat{h}_\sigma \hat{\varphi} (A + \hat{a}) [\partial_\varphi \mathcal{D}_e^A - i \mathcal{A}_{AA} \mathcal{D}_e^A] \end{aligned} \quad (\text{B6})$$

Here in the third line we employed our assumptions that $\hbar\nu, \hbar\nu_{ph} \approx E_0 + E_F + E_A$ up to a detuning much smaller than $(E_A - E_{\beta \neq A}) \sim \Delta$, and $\omega_m \ll E_{\beta \neq A} \sim \Delta$. Furthermore, in the last line we used the identity

$$i \sum_{\beta} (\mathcal{A}_{A\beta} \mathcal{D}_e^\beta - \mathcal{B}_{A\beta}^* \mathcal{D}_h^\beta) = \frac{\partial}{\partial \varphi} \mathcal{D}_e^A, \quad (\text{B7})$$

that is guaranteed by gauge invariance and can be verified by substituting Eqs. (5) and (B3). The resulting last bracket is gauge invariant, but we may specialize to the so-called parallel transport gauge, in which the diagonal connections are fixed to zero, $\mathcal{A}_{\alpha\alpha} = 0$. Dropping the A index of the remaining ABS, this gives the compact effective term

$$\hat{H}_{\text{eff}} = \sum_{\sigma} \hat{\gamma}_{\sigma}^\dagger \hat{h}_{\sigma} (\partial_\varphi \mathcal{D}_e) \hat{\varphi} (A + \hat{a}) \quad (\text{B8})$$

which we incorporate into Eq. (7) in the main text.

Appendix C: Additional parameter combinations

The results we present in the main text are qualitatively unchanged as the junction parameters are varied. However, quantitative magnitude of our results is somewhat sensitive to these parameter values. In this Appendix we present this dependence for completion.

The most tunable quantity is $\mathcal{D}_{e,h}/g$, which is determined by the wavefunction overlap between the trapped valence hole and the Andreev electron and hole components. Since the ABS and valence states have disparate momentum contents, their overlap can depend interferometrically on geometric details. Therefore, the most sensitive knobs for influencing $\mathcal{D}_{e,h}$ are the junction geometric length L and position of the trapping potential $L_Z \in [-L/2, L/2]$ within it.

In Figs. 4 and 5 we present the absorption spectrum and transduction amplitudes, counterpart to Figs. 2 and 3, for various combinations of L and L_Z (measured as a fraction of L). As we see, the behavior we describe in the text is quite general for most parameter combinations. To reiterate these are: The absorption spectrum has two resonance lines that stand out from valence band-edge transitions, and either transduction amplitude is nonzero for all junction phase biases.

However, quantitative differences can also be gleaned. $L_Z = 0$ (left column of panels) gives a spurious inversion symmetry (see previous sections) which causes $\mathcal{D}_h(\varphi = \pi)$ to vanish, as well as the transduction coefficients $\propto \partial_\varphi \mathcal{D}_e(\varphi = 0, \pi)$. Furthermore, the length dependence can lead to strong suppression of the dipole transition at fine-tuned points. For example, with $L = 360$ nm and $L_Z = 0$, this is evidenced in a $\sim 10^{-4}$ suppression of the transduction coefficients; as a result the resonant absorption lines are drowned by transitions from the valence band continuum.

Similarly, also at $L = 360$ nm but $L = L_Z/10$, we see an atypical inversion of the relative absorption intensities: The anomalous absorption line (concave curve) is brighter than the normal absorption line (convex curve).

Finally, the contribution of the valence band continuum also changes somewhat: While for some combinations (e.g. $L = 580$ nm) this background contribution is roughly constant, at other combinations (e.g. $L = 690$ nm, and especially in the $L_Z = L/4$ case) there is strong enhancement from the continuum edge. Yet in all these cases the resonant lines generally remain resolvable.

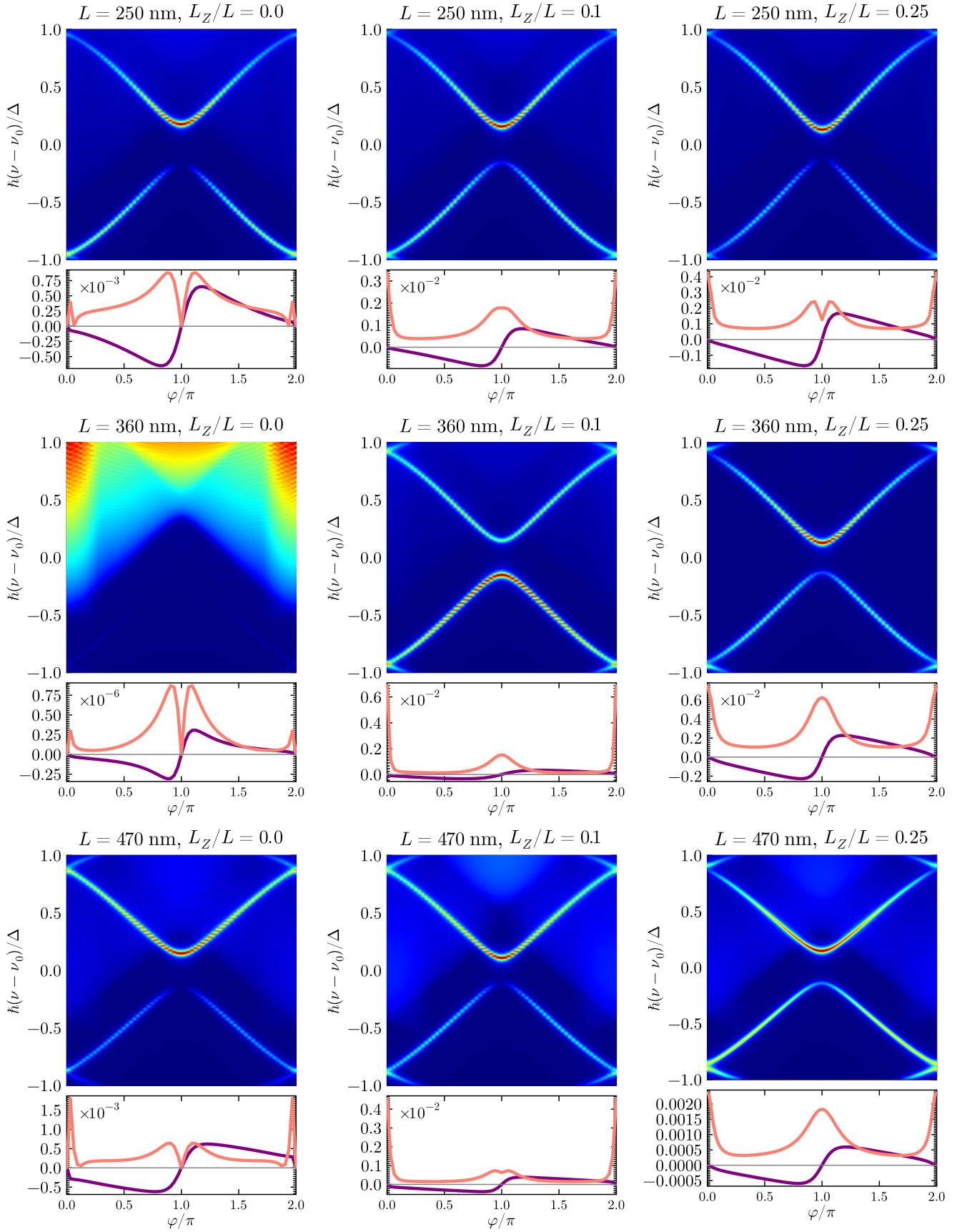


FIG. 4. Absorption spectra and transduction amplitudes versus phase, for the indicated junction length L and barrier position L_Z . The top right panel is a reproduction of Figs. 2 and 3 of the main text. Other parameters same as in the main text. Note the absorption color scale is not shared across panels.

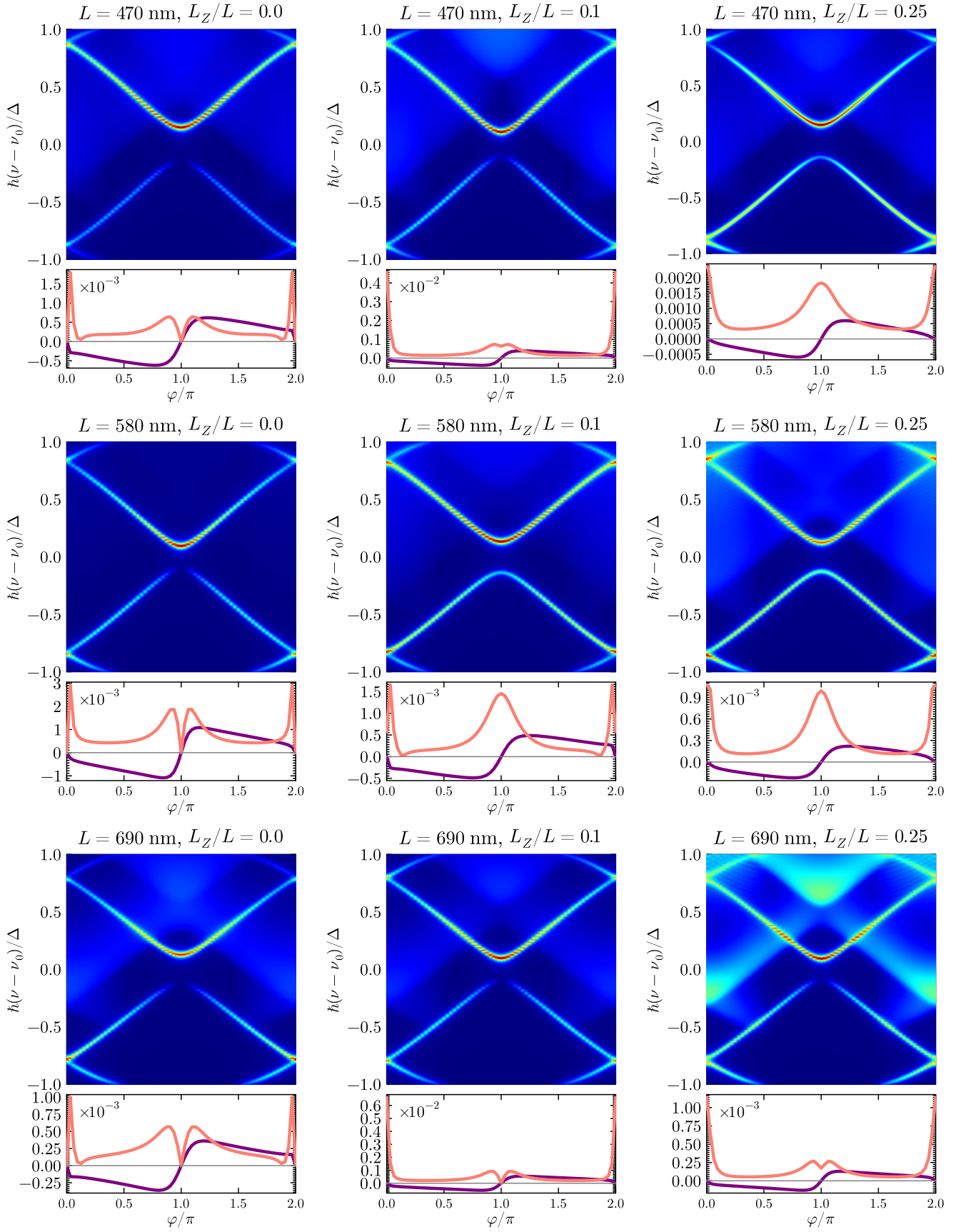


FIG. 5. Continuation of Fig. 4.